ON THE ASYMMETRY OF THE OH RO-VIBRATIONAL LINES IN HD 100546*

D. Fedele[1], S. Bruderer[1], M. E. van den Ancker[2], and I. Pascucci[3]

[1] Max Planck Institut für Extraterrestrische Physik, Giessenbachstrasse 1, D-85748 Garching, Germany; fedele@mpe.mpg.de
[2] European Southern Observatory, Karl Schwarzschild Strasse 2, D-85748 Garching bei München, Germany; mvandena@eso.org
[3] Lunar and Planetary Laboratory, The University of Arizona, Tucson, AZ 85721, USA; pascucci@lpl.arizona.edu

ABSTRACT

We present multi-epoch high-spectral resolution observations with VLT/CRIRES of the OH doublet $^2\Pi_{3/2}$ P4.5 (1+, 1−) (2.934 μm) toward the protoplanetary disk around HD 100546. The OH doublet is detected at all epochs and is spectrally resolved while nearby H_2O lines remain undetected. The OH line velocity profile is different in the three data sets: in the first epoch (2012 April , P.A. = 26°) the OH lines are symmetric and line broadening is consistent with the gas being in Keplerian rotation around the star. No OH emission is detected within a radius of 8–11 AU from the star: the line emitting region is similar in size and extent to that of the CO ro-vibrational lines. In the other two epochs (2013 March and 2014 April, P.A. = 90° and 10°, respectively) the OH lines appear asymmetric and fainter compared to 2012 April. We investigate the origin of these line asymmetries which were taken by previous authors as evidence for tidal interaction between a (unseen) massive planet and the disk. We show that the observed asymmetries can be fully explained by a misalignment of the slit of the order of 0″.04–0″.20 with respect to the stellar position. The disk is spatially resolved and the slit misalignment is likely caused by the extended dust emission which is brighter than the stellar photosphere at near-infrared wavelengths which is the wavelength used for the pointing. This can cause the photo-center of HD 100546 to be misaligned with the stellar position at near-infrared wavelengths.

Key word: protoplanetary disks

1. INTRODUCTION

HD 100546 is a 2.4 $M_\odot$ pre-main-sequence star surrounded by a gas- and dust-rich protoplanetary disk. The inner region of the disk ($r \lesssim 10$ AU) is devoid of molecular gas (van der Plas et al. 2009; Brittain et al. 2009) while atomic gas is still present in this gap (Acke & van den Ancker 2006). Emission by small dust grains is detected in the vicinity of the star ($r < 4$ AU; Benisty et al. 2010) while no small grains are detected outward up to ∼13 AU from the star (e.g., Bouwman et al. 2003; Tatulli et al. 2011; Panić et al. 2014). The lack of molecular gas is likely due to photo-dissociation of molecules which, given the reduced amount of small dust grains, are not shielded from the dissociative radiation of the star (e.g., Bruderer 2013). Liskowsky et al. (2012) and Brittain et al. (2014) detect OH ro-vibrational emission (doublets $^2\Pi_{3/2}$ P10.5 and P9.5) toward this source using PHOENIX at the Gemini South telescope. The OH lines show a highly asymmetric velocity profile deviating from the characteristic symmetric double-peaked Keplerian profile: the blueshifted peak is stronger than the redshifted one. Liskowsky et al. (2012) and Brittain et al. (2014) interpret the asymmetric OH profile as due to gas emission in a highly eccentric orbit ($e \gtrsim 0.18$) from the tidal interaction between a massive planet and the disk. Theoretical calculations (e.g., Lubow 1991) and hydrodynamical simulations (e.g., Kley & Dirksen 2006) show indeed that a stellar companion or massive planet is able to perturb the orbital motion of the gas and this produces an asymmetric velocity profile of the molecular gas orbiting around the star (Regály et al. 2010). Observationally, this effect was detected, e.g., toward the protoplanetary disk around V380 Ori (Fedele et al. 2011), where the OH P4.5 line

profile is asymmetric. The origin of this asymmetry is most likely the stellar companion of V380 Ori which perturbs the gas motion in the inner disk.

In the case of HD 100546, however, no stellar companion has been detected so far inside the dust gap (e.g., Grady et al. 2005), and the disk eccentricity must be caused by a massive (unseen) planetary companion inside the dust gap. No line asymmetry has been reported for the CO ro-vibrational lines (which trace similar radial distances as the OH ro-vibrational lines) toward the same disk by several authors (van der Plas et al. 2009; Brittain et al. 2009; Goto et al. 2012; Liskowsky et al. 2012; Brittain et al. 2013). Hein Bertelsen et al. (2014) re-observed HD 100546 with CRIRES and they found that the line profile of CO ro-vibrational transitions vary (become asymmetric) with the slit position angle (P.A.) and with time (timescale of two nights). According to Hein Bertelsen et al. (2014), this is due to a small ($\gtrsim 0″.1$) offset of the slit with respect to the barycenter of the system; note that at a distance of 97 pc (van Leeuwen 2007) the inner disk of HD 100546 is spatially resolved with an 8 m class telescope at near-infrared wavelengths (e.g., Goto et al. 2012).

This paper presents multi-epoch high-spectral resolution observations with VLT/CRIRES of the OH ro-vibrational lines $^2\Pi_{3/2}$ P4.5 (1+,1−) at 2.934 μm toward HD 100546. The goal is to investigate the origin of the asymmetry in the OH ro-vibrational lines as reported by Liskowsky et al. (2012) and Brittain et al. (2014).

2. OBSERVATIONS AND DATA REDUCTION

HD 100546 was observed in the *L* band at three different epochs with VLT/CRIRES spanning two years (2012 April, 2013 March, 2014 April). Each observation of HD 100546 is followed by that of a standard star of early spectral type for the removal of telluric absorption features. The 2012 and 2014

Table 1
Observations Log

Date	Time (UT)	$\lambda_{\rm ref}$ (nm)	Slit Width ($''$)	Slit P.A. ($°$)	PSF ($''$)	Δv (km s^{-1})	DIT (s)	NDIT	STD	PSF (STD) ($''$)
2012 Apr 2	04:54:05	2911.5	0$''$2	26$°$	0$''$17[a]	3.5	30	2	HIP 57936	0.14
2013 Mar 18	23:38:37	2947.0	0$''$4	90$°$	0$''$65	5.3	30	4	HIP 60718	0.63
2014 Apr 17	03:05:23	2950.0	0$''$2	10$°$	0$''$17[a]	3.5	60	1	HIP 57851	0.15

Note. [a] Adaptive optics supported. P.A. equal to the parallactic angle.

spectra were taken with a 0$''$2 slit width and are supported by the CRIRES adaptive optics system using the target as adaptive optics (AO) wavefront sensor and slit viewer guide star. The slit was oriented along the parallactic angle to minimize slit losses due to atmospheric refraction. The spectral resolution, measured on the OH sky emission lines is 3.5 km s^{-1} and the FWHM of the target is $\sim$0$''$17. The FWHM of the telluric standard star is $\sim$0$''$13, thus HD 100546 is spatially resolved. The 2013 spectrum (also presented in Brittain et al. 2013) was taken with a slit width of 0$''$4 at a position angle of P.A. = 90$°$ (different from the parallactic angle) without adaptive optics. In this case the spectral resolution is 5.3 km s^{-1} and the FWHM (the seeing) is 0$''$65, thus the spectrum is affected by slit losses. At all epochs the centering of the target in the slit is done through the slit-viewer camera in the K_s band. The observation log is reported in Table 1.

The spectra are reduced with the CRIRES data reduction pipeline using a standard procedure: bad-pixel and cosmic rays subtraction, flat-fielding, wavelength calibration (using the sky emission lines as reference), and spectrum extraction. The telluric absorption lines are removed by dividing the spectrum of HD 100546 with that of the telluric standard after applying small correction to account for the slightly different optical depth of the telluric lines between the two spectra. Figure 1 shows the spectrum of the OH doublet at the three epochs.

2.1. Pointing and Guiding Accuracy

For CRIRES, the centering of point-sources within the slit is known to be accurate to a small fraction of the slit width: according to the CRIRES User Manual[4] the pointing and guiding accuracy is, on average of the order of 0.2 pixels (for the 0$''$2 slit with adaptive optics), which corresponds to 0$''$017 at a pixel scale of 0$''$086. We estimated the pointing accuracy directly from the offset applied to the telescope during the guiding (log files provided by J. Smoker and the ESO user support department). We find an accuracy of 0$''$03 for the two AO-fed observations and 0$''$14 for the non-AO one. Thus, as expected, the pointing and guiding accuracy is more accurate in the AO-supported observations.

2.2. Flux Calibration

The telluric standard stars are also used to calibrate the continuum flux of HD 100546 in a region free of telluric absorptions. The spectra extracted from the CRIRES data reduction pipeline are divided by the DIT of the exposure (Table 1). For each telluric standard we estimate the absolute spectrophotometric flux ($F_{\lambda,0}^{\rm kur}$) by scaling the corresponding Kurucz stellar atmosphere model to the Two Micron All Sky Survey J, H, and K magnitude of the star. The transmission

Table 2
Multi-epoch 3 μm Flux of HD 100546

Epoch	F_ν (Jy)	$\lambda_{\rm ref}$ (μm)	Reference
1989–1992	5.5	3.7	Malfait et al. (1998a; L-band photometry)
1998	5.44 $\pm$ 0.06	2.934	Malfait et al. (1998b; ISO spectrum)
2010	6.2 $\pm$ 0.6	3.353	$WISE$ W1 photometry
2012	4.5 $\pm$ 1.0	2.934	This work
2013	5.0 $\pm$ 1.0	2.934	This work
2014	5.0 $\pm$ 1.0	2.934	This work

function (instrument + atmosphere) T_λ is given by the ratio of the observed (in units of ADU s^{-1}) and absolute flux (Wm$^{-2}\mu$m^{-1})

$$T_\lambda = \frac{F_\lambda^{\rm obs}({\rm STD})}{F_{\lambda,0}^{\rm kur}({\rm STD})}. \quad (1)$$

The science spectrum is then flux calibrated as follow:

$$F_{\lambda,0}({\rm SCI}) = \frac{F_\lambda^{\rm obs}({\rm SCI})}{T_\lambda}, \quad (2)$$

where $F_\lambda^{\rm obs}({\rm SCI})$ is the observed flux after normalization for exposure time (ADU s^{-1}). The continuum flux of HD 100546 is then measured at $\lambda = 2934.63$ nm, next to the OH doublet, in a region free of telluric absorption. Results are listed in Table 2 for the three epochs.

The accuracy of the method was tested using the CRIRES spectra of telluric standard stars observed on a different night (2008 December 5). Multiple (nine) standard stars were observed during the night allowing us to estimate the validity and precision of the flux calibration method. The spectra are presented in Fedele et al. (2011).

Following the same procedure, the absolute flux of each star is estimated by scaling the Kurucz atmosphere model to the J, H, and K magnitudes ($F_{\lambda,0}^{\rm kur}({\rm STD})$). The transmission function is measured as in Equation (1) using one of the nine stars. The remaining eight stars are flux calibrated using Equation (2), yielding $F_{\lambda,0}({\rm STD})$. For each star, we measure the flux difference at $\lambda = 2934.63$ nm as the difference:

$$\Delta {\rm F}({\rm STD}) = {\rm ABS}\left(\frac{{\rm F}_0^{\rm kur}({\rm STD}) - {\rm F}_0({\rm STD})}{{\rm F}_0^{\rm kur}({\rm STD})}\right). \quad (3)$$

The result is shown in Figure 2 for the different standard stars as a function of observing time (the airmass varies between 1.03 and 1.46). The flux difference ranges between $\sim$10%–40% with an average value of 20%. Thus the flux calibration method of the CRIRES spectra performed using the telluric standard stars has, on average, an accuracy of 20%.
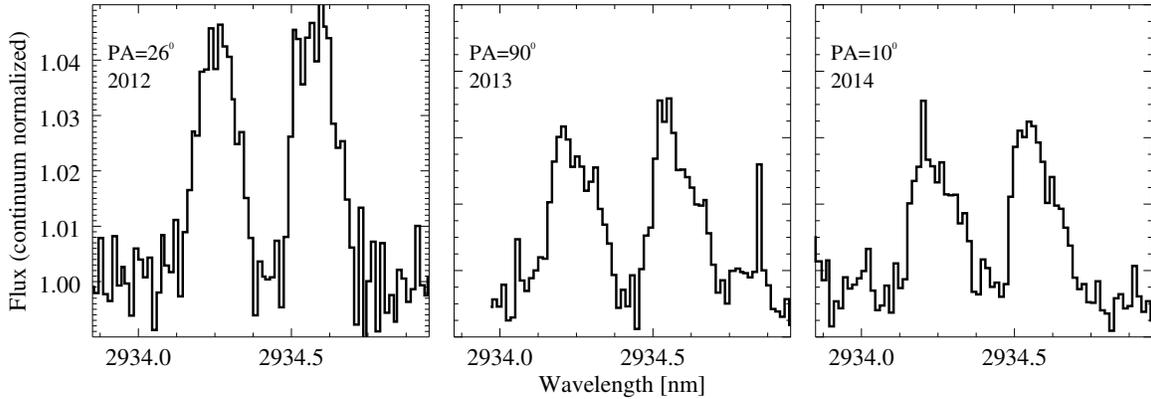

Figure 1. CRIRES spectra of the OH doublet $^2\Pi_{3/2}$ P4.5 toward HD 100546 at three different position angles (and epochs).
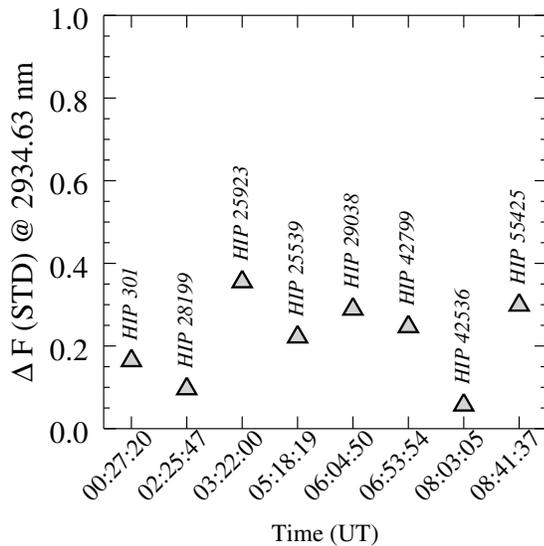

Figure 2. Accuracy of the flux calibration method described in Section 2.

Table 3
OH Line Flux for HD 100546

Epoch	W(OH)[a] $(10^{-6}\ \mu\mathrm{m})$	F(OH) $(10^{-18}\ \mathrm{W\,m^{-2}})$
2012 Apr 2	7.2 ± 0.4	11.1 ± 0.6[b]
2013 Mar 18	4.3 ± 0.3	7.4 ± 0.5[b]
2014 Apr 17	3.9 ± 0.3	6.7 ± 0.5[b]

Notes.
[a] The value of equivalent width is the average of the two transitions and the error is given by the difference of the two.
[b] The error does not include the 20% flux calibration uncertainty.

3. RESULTS

3.1. Line Detection

The OH $^2\Pi_{3/2}$ P4.5 doublet is detected in all three epochs (Figure 1) while H_2O is undetected, confirming the trend of high OH/H_2O abundance ratio in the atmosphere of the inner disk of Herbig AeBe systems (Mandell et al. 2008; Pontoppidan et al. 2010; Fedele et al. 2011). In all cases the lines are spectrally resolved. In 2012 April the two OH lines are symmetric contrary to what found by Liskowsky et al. (2012) in their PHOENIX spectrum (from 2010). In the other two epochs, the lines are asymmetric.

The equivalent width (W) is measured by integrating over the velocity range between $-20\,\mathrm{km\,s^{-1}}$ and $+20\,\mathrm{km\,s^{-1}}$. The values of W reported in Table 3 refer to the average value of the two transitions and the error is measured as the difference between the two. The line flux is measured by multiplying W by the continuum flux next to the line at $\lambda = 2934.63$ nm. The equivalent width (hence the line flux) varies considerably among the three epochs with the OH line being the strongest in 2012 when the velocity profile is symmetric.

3.2. Continuum Emission

The continuum flux next to the line is constant among the three epochs (Table 3). Multi-epoch 3 μm flux measurements of HD 100546 are listed in Table 2. Our estimates are in good agreement with the *Infrared Space Observatory* (*ISO*) spectrum (e.g., Malfait et al. 1998b) which shows a flux density of 5.45 Jy (± 0.06 Jy) at the same reference wavelength ($\lambda = 2934.63$ nm). The *L*-band magnitude reported by Malfait et al. (1998a) is 4.15 mag (no error given) which corresponds to a flux density of 5.5 Jy at $\lambda_e = 3.7\ \mu$m (adopting a zero magnitude star flux $F_0 = 253$ Jy; Le Bertre & Winters 1998). The *Wide-field Infrared Survey Explorer* (*WISE*) W1 magnitude is 4.2 ± 0.1 mag Cutri et al. (2012) which yields $F_\nu = 6.2 \pm 0.60$ Jy (after color correction using the *ISO* spectrum) at $\lambda_e = 3.353\ \mu$m. We note that the *WISE* photometry is likely affected by the strong polycyclic aromatic hydrocarbon feature between 3 and 3.5 μm (see, e.g., Malfait et al. 1998b). Indeed, the *WISE* W1 synthetic photometry computed by convolving the *ISO* spectrum with the W1 bandpass (Wright et al. 2010) gives a flux density of $F_\nu = 5.75$ Jy, closer to the photometric measurement.

In conclusion, our estimate of the continuum flux is in good agreement with the *ISO* spectrum and with the broadband photometry measured by Malfait et al. (1998a) and more recently with *WISE*. These results do not confirm the 50% decrease of the *L*-band flux found by Brittain et al. (2013) between ~1990 and 2010.

4. ANALYSIS

The following analysis is divided in two parts. First, we analyze the OH line to derive the line emitting region and to search for similarities/differences with respect to other gas
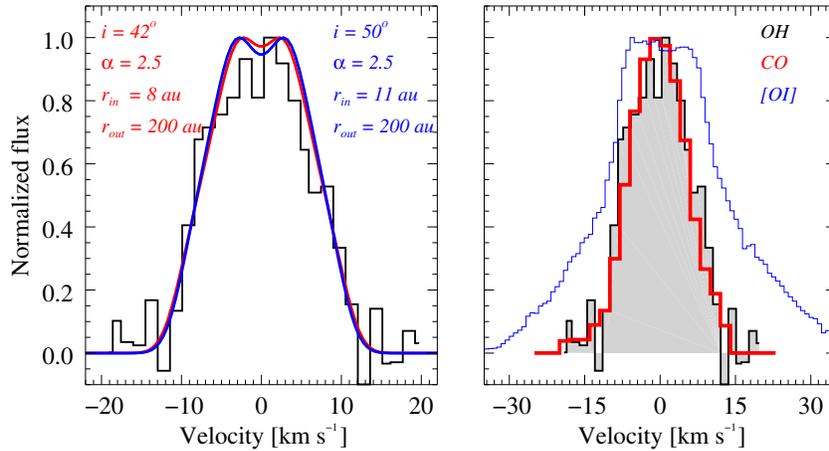
Figure 3. Left: OH P4.5 line velocity profile (average of the two transitions at P.A. = 26°) and best-fit models (solid curves) for a disk inclination of 42° (red) and 50° (blue), respectively. Right: comparison of the line profiles of different gas tracers: OH (P.A. = 26°), CO (median profile of fundamental ro-vibrational lines, P.A. = 55°), and [O I] 630.0 nm (P.A. = 15°).

tracers. Then, we investigate the origin of the asymmetric OH line profiles seen in some but not all data sets.

4.1. OH Emitting Region

To estimate the line emitting region, we create a synthetic profile assuming a power-law intensity profile:[5]

$$I(r) = I(r_{in}) \cdot (r/r_{in})^{-\alpha}, \qquad (4)$$

where r is the distance from the star and $I(r_{in})$ is the intensity at the inner radius. Equation (4) is converted into a line velocity profile: assuming Keplerian rotation the projected velocity is

$$v_{proj}(r, \theta, i) = \sqrt{\frac{GM_*}{r}} \sin(i) \cos(\theta) \qquad (5)$$

with i the disk inclination ($i = 0°$ is edge on). The OH temperature is fixed to 1100 K, similar to the CO temperature at the inner rim of the disk, ∼10 AU (e.g., Goto et al. 2012; Fedele et al. 2013). This temperature corresponds to a thermal broadening $v_{th} = \sqrt{2kT/m_{OH}} = 1.2 \text{ km s}^{-1}$. The velocity profile is convolved with a velocity width $v = \sqrt{v_{in}^2 + v_{th}^2}$ with v_{in} the instrumental broadening (Table 1).

To find the best-fit model, the observed velocity profile is fitted by a synthetic profile. The parameters of the fit are (1) the power-law index of the intensity α, (2) the disk inclination, and (3) the inner and (4) outer radius of the OH emitting region. The disk inclination and inner radius are partly degenerate, for this reason we fix the inclination and let the other parameters free. To search for the best-fit parameters we create a grid of model line profiles varying α (range 1.5–4, step 0.025), r_{in} (range 5–15 AU, step 0.1 AU) and r_{out} (range 30–230 AU, step 20 AU) and we compute the reduced χ^2 between the observed and model line profile. The set of parameters that best fit the observed profile are found minimizing $\tilde{\chi}^2$

$$\tilde{\chi}^2 = \frac{1}{N-1-n} \Sigma_i \left(\frac{m_i - f_i}{\sigma_i} \right)^2 \qquad (6)$$

with N the number of velocity bins in the range between -25 km s^{-1} and $+25 \text{ km s}^{-1}$, n the number of parameters (=4),

---

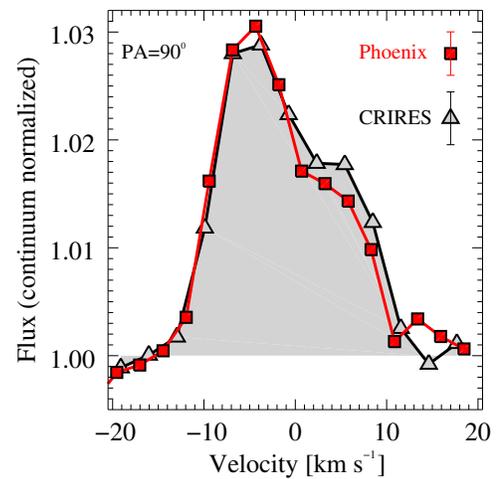[5] The formalism is described in Fedele et al. (2011).

Figure 4. Comparison of CRIRES and PHOENIX spectra at P.A. = 90°. The average of the two P4.5 transitions (1+, 1−) is shown for the CRIRES spectra while the PHOENIX spectrum is the average of the four lines detected by Liskowsky et al. (2012; doublet P9.5 and P10.5). In all the spectra the continuum is normalized to unity.

m_i and f_i the model predicted and observed flux at velocity bin i, and σ_i the corresponding uncertainty. The fitting procedure is repeated twice for two different values of the inclination, 42° and 50°, since all inclinations reported in the literature are within this range (Pantin et al. 2000; Augereau et al. 2001; Grady et al. 2001; Liu et al. 2003; Ardila et al. 2007; Panić et al. 2014; Avenhaus et al. 2014). The parameters that best fit the observed profile are listed in Figure 3 together with the best-fit models: for the $i = 42°$ case we find an inner radius of 8 AU ($\tilde{\chi}^2 = 1.02$), while for the $i = 50°$ case we find an inner radius of 11 AU ($\tilde{\chi}^2 = 1.03$).

The lack of high-velocity gas indicates a gap (drop in abundance) of OH gas inside a gap of radius ∼8–11 AU (depending on the assumed inclination).

4.2. Comparison of CRIRES and PHOENIX OH Profile

Figure 4 shows a direct comparison of the CRIRES and PHOENIX spectra (presented in Liskowsky et al. 2012) taken with the same slit position angle (90°) and width (0″4): to increase the signal-to-noise ratio (S/N) we averaged the two lines of the OH P4.5 doublet (CRIRES), while the PHOENIX

spectrum is the average of the four lines detected by Liskowsky et al. (doublets P9.5 and P10.5). Finally, the spectra are binned in wavelength to further increase the S/N. The two spectra are similar. There are however some differences: the peak-to-peak asymmetry appears more pronounced in the PHOENIX spectrum, where the redshifted component is systematically fainter than in the CRIRES spectra. This difference is significant as it is seen in several (consecutive) spectral bins.

4.3. Comparison to Other Gas Tracers

In this section, we compare the velocity profile of the OH P4.5 doublet to that of other gas tracers, namely the CO ro-vibrational lines and the optical forbidden line [O I] 630.0 nm. The median profile of the CO fundamental ro-vibrational transitions (v = 1–0, 2–1, 3–2, and 4–3) is shown in Figure 3 (right). These spectra were taken with CRIRES with a spectral resolution of $\sim$3 km s^{-1} (slit width = 0$''$2, P.A. = 55$°$, PSF = 0$''$17, 2010 March 29; Hein Bertelsen et al. 2014). The similarity of the velocity profiles of the OH (P.A. = 26$°$) and CO ro-vibrational lines and the symmetric profile of CO suggests that these transitions come from a similar radial extent in the disk. The inner radius of the OH emitting region found here is in good agreement with r_{in}(CO) from previous estimates: r_{in}(CO) = 8 AU (van der Plas et al. 2009, i = 42), r_{in}(CO) = 13 AU (Brittain et al. 2009, i = 50).

The spectrum of the [O I] 630.0 nm line is also shown in Figure 3 (VLT/UVES, P.A. = 15$°$, slit width = 0$''$3, Acke & van den Ancker 2006). The oxygen line extends to high velocity indicating the presence of atomic gas inside the disk gap. The low-velocity part of the [O I] line appears slightly asymmetric and both the asymmetry and the line intensity vary with time according to Acke & van den Ancker (2006). The asymmetry in the [O I] line is however much less pronounced than that of the OH P4.5 lines at slit P.A. = 10$°$ and 90$°$. Moreover, the temporal changes reported by Acke & van den Ancker (2006) are not reconcilable with the changes in the OH line as the OH asymmetry is only observed in the blueshifted peak, contrary to the [O I] where the asymmetry is observed also in the redshifted peak. For further discussion, see Section 5.

4.4. Line Asymmetry

As shown by Hein Bertelsen et al. (2014), in the case of spatially resolved observations, a slight offset can induce slit losses in the CO ro-vibrational lines and produce an asymmetric line profile. Given the similar size and extent, the OH ro-vibrational lines may also be affected by the same process. The different flux of the OH line between the three epochs can be the consequence of slit losses. If this is the case the 2012 spectrum, showing the higher line flux, is the less affected one. To investigate this, we create a synthetic disk image using a geometrical model where the OH line is assumed to emerge from either the surface or an inner wall of a disk in Keplerian rotation. The intensity on the surface and the wall are taken to be the same. Figure 5 shows the synthetic velocity map. The figure also shows the width and orientation of the three CRIRES OH spectra. The synthetic disk image is convolved with a 2-D Gaussian profile to mimic the point spread function (PSF) of the CRIRES spectra. The FWHM of the convolution is given by the actual size of the target in the spatial direction of the spectrum (Table 1): this corresponds to 0$''$17 for the spectra taken with the 0$''$2 slit (P.A. = 26$°$ and 10$°$) and 0$''$65 in the case of the 0$''$4 slit (P.A. = 90$°$). The synthetic line profiles are created by filtering
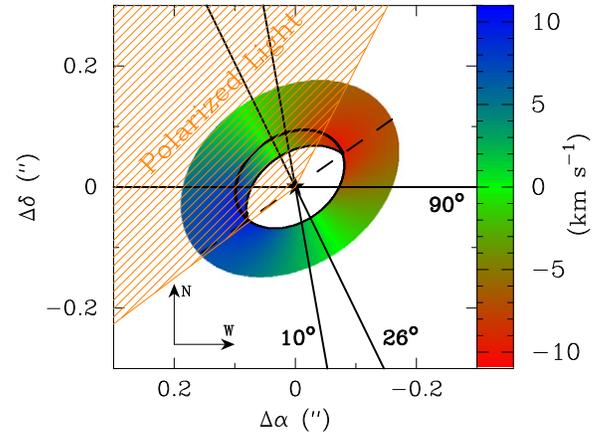

Figure 5. Synthetic OH velocity map. The dashed line shows the position angle of the disk's major axis (145$°$, Ardila et al. 2007). The slit position angles at the three epochs are also shown. The dashed region shows the side of the disk which appears brighter in polarized light from Quanz et al. (2011) and Avenhaus et al. (2014).

the convolved disk images with the corresponding slit width and position angle. The effect of a slit misalignment is reproduced by an offset between the slit and the stellar position in the direction perpendicular to the slit P.A. The sign convention for the offset is the same as in Hein Bertelsen et al. (2014). Finally, the synthetic line profiles are convolved with the corresponding spectral resolution: 3.5 km s^{-1} and 5.3 km s^{-1} for the 0$''$2 and 0$''$4 slit width, respectively (Table 1).

Figure 6 shows the synthetic spectra for different offsets in the cases of P.A. = 10$°$ and P.A. = 90$°$: the offset produces an asymmetry in the line profile, and the flux ratio between the blueshifted and redshifted component of the OH line increases with the offset. For a given offset, the asymmetry is more pronounced in the narrow slit spectrum. This is due to the different size of the PSF. The spectra are normalized although the offset induces slit losses which results in a fainter line flux as the offset increases. A small offset (between $-0''$04 and $-0''$06) is enough to reproduce the observed profile at P.A. = 10$°$, while a larger offset (between $-0''$16 and $-0''$20) is needed for the P.A. = 90$°$ spectrum.

5. DISCUSSION

The analysis presented here demonstrates that the asymmetric profile of the OH ro-vibrational lines are consistent with an offset between the slit and the stellar position. Our interpretation is that the spectra which are mostly affected by the slit misalignment are the P.A. = 10$°$ and P.A. = 90$°$ (both CRIRES and PHOENIX). The P.A. = 26$°$ spectrum indeed shows no clear evidence of asymmetry in the line profile which appears instead top-flat as we would expect in the case of Keplerian rotation. Moreover, in the same spectrum the line is much stronger (almost double, Table 1) than in the other spectra. This finding suggests that the P.A. = 10$°$ and P.A. = 90$°$ spectra can be affected by slit losses which is a natural consequence of the slit misalignment. The small offsets estimated in the previous section produce negligible or no change of the continuum flux but considerable variation of the OH line velocity profile.

5.1. Origin of the OH Line Asymmetry

If the asymmetric profile of the OH line is due to an offset of the slit, this must be caused by the source itself as it is observed
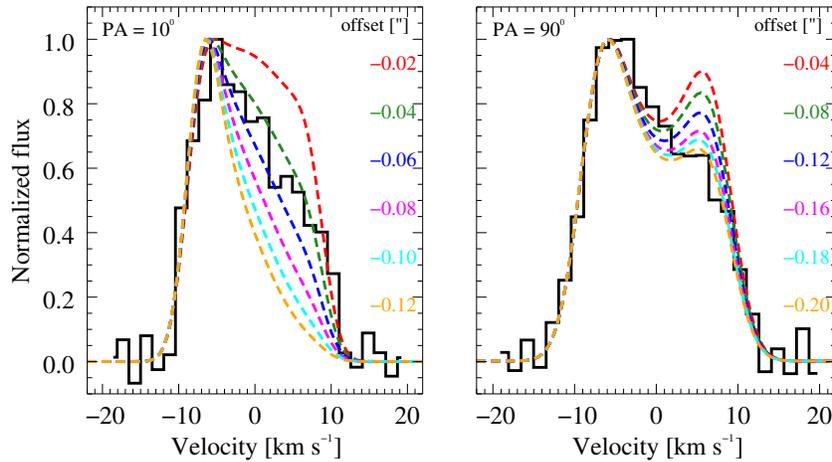
Figure 6. Comparison of the P.A. = 10° (left) and P.A. = 90° (right) CRIRES OH spectra (average profile of the 1+ and 1− transitions) with synthetic profiles with different offset between the slit position and the central star (see Section 4.4).

with two different instruments (CRIRES and PHOENIX). A possible explanation is that the misalignment of the slit is caused by a non-homogenous illumination: we infer that this is due to the finite size of the disk inner wall ∼10 AU from the star. Because of the disk inclination (∼42°–50°), the inner wall at 10–14 AU produces an asymmetric image in the sky (see Figure 5). Interestingly, deviation from axisymmetric emission is detected in mid-infrared interferometric observations (Panić et al. 2014). Given the higher intensity of the disk wall over the stellar photosphere at wavelength >1 μm, the peak of the continuum intensity at these wavelengths does not coincide with the stellar position. Since the telescope pointing is automatically adjusted toward the peak of the emission in the K_s band in the slit viewer camera,[6] this can affect the centering of the target inside the slit, inducing an offset between the center of the slit and the stellar position. The misalignment of the slit should be maximum when the slit P.A. is parallel to the disk's major axis (∼130°–160°; e.g., Pantin et al. 2000; Augereau et al. 2001; Grady et al. 2001; Ardila et al. 2007; Panić et al. 2014; Avenhaus et al. 2014) and it should be minimized when the slit is oriented along the disk minor axis. This is consistent with the different offset measured in the P.A. = 90° and P.A. = 10° spectra and with the symmetric profile seen in the P.A. = 26° (closer to the disk minor axis) spectrum.

Our interpretation is supported by the polarimetric differential imaging of HD 100546 performed by Quanz et al. (2011) and Avenhaus et al. (2014): the authors detect a brightness asymmetry in polarized light with the northeast part (far side) of the disk being brighter than the southwestern one (near side). The azimuthal directions of this asymmetry is shown in Figure 5.

We further note that our interpretation is in good agreement with near-infrared interferometric observations (Benisty et al. 2010; Tatulli et al. 2011): the K-band VLTI/AMBER visibility at short baselines can only be fitted by a model which includes spatially extended emission, consistent with the disk inner wall at ∼13 AU (Tatulli et al. 2011).

5.2. Disk Wall or Clumps

There are other possible scenarios that can induce a slit offset: any bright source (brighter than the star in the K band) within ∼0″2 from the star could induce a misalignment of the

slit during the acquisition of the spectrum. One possibility is a stellar companion, there are however no detections of any bright companion within 0″2 to date. Another possibility is inhomogeneous dust continuum emission from the disk. Recent polarimetric observations by Avenhaus et al. (2014) rule out the presence of a disk hole at P.A. = 12° claimed by Quanz et al. (2011) while they detect two bright spots at P.A. ∼ −30° and P.A. ∼ 130° with the latter being brighter than the first one. We warn however that the spots seen in polarized light do not necessarily imply the existence of bright spots in the total (unpolarized) K-band flux. The results of Quanz et al. (2011) and Avenhaus et al. (2014) are instead consistent with the overall geometry of the disk where the northeast side (brighter in scattered light) is facing toward us.

5.3. Disk Eccentricity

Liskowsky et al. (2012) suggest that the inner disk of HD 100546 is eccentric and the OH distribution is not homogeneous: the authors propose a scenario in which a massive (unseen) planet perturbs the gas dynamics at the distance of the disk inner wall. Brittain et al. (2014) further support this scenario based on the non-variability of the OH line profiles: the OH spectra presented by Brittain et al. (2014) are both taken with the same slit P.A. (=90°). As shown in Figure 4 however, the P.A. = 90° spectra (CRIRES and PHOENIX) do show a slightly different line profile, which cannot be due to disk eccentricity. Moreover, the P.A. = 10° and P.A. = 26° spectra show drastic variation in line profile and equivalent width.

Brittain et al. (2014) assume an eccentricity of 0.18 (±0.11) to explain the asymmetry of the OH lines. However, no evidence for disk eccentricity was found in the differential polarimetric observations of Avenhaus et al. (2014; e < 0.133 at 99.8% confidence).

6. CONCLUSION

Based on the data collected here and on the performed analysis, the asymmetric profile of the OH ro-vibrational lines toward HD 100546 are consistent with a misalignment of the slit of the order of 0″04–0″2. We argue that the misalignment results from the finite size of the disk inner wall at ∼10–14 AU from the star (∼0″10–0″14 at a distance of 97 pc). Thus there is no need to invoke a highly eccentric gas disk, as was done by Liskowsky et al. (2012) and Brittain et al. (2014), to explain the

---

[6] Note that the star itself is occulted by the slit in the SV camera.

asymmetric line profile in HD 100546. The analysis presented in this paper, however, does not exclude the presence of a massive planet/companion inside the disk gap as suggested by several authors (e.g., Bouwman et al. 2003; Acke & van den Ancker 2006; Mulders et al. 2013).

REFERENCES

Acke, B., & van den Ancker, M. E. 2006, A&A, 449, 267
Ardila, D. R., Golimowski, D. A., Krist, J. E., et al. 2007, ApJ, 665, 512
Augereau, J. C., Lagrange, A. M., Mouillet, D., & Ménard, F. 2001, A&A, 365, 78
Avenhaus, H., Quanz, S. P., Meyer, M. R., et al. 2014, ApJ, 790, 56
Benisty, M., Tatulli, E., Ménard, F., & Swain, M. R. 2010, A&A, 511, A75
Bouwman, J., de Koter, A., Dominik, C., & Waters, L. B. F. M. 2003, A&A, 401, 577
Brittain, S. D., Carr, J. S., Najita, J. R., Quanz, S. P., & Meyer, M. R. 2014, ApJ, 791, 136
Brittain, S. D., Najita, J. R., & Carr, J. S. 2009, ApJ, 702, 85
Brittain, S. D., Najita, J. R., Carr, J. S., et al. 2013, ApJ, 767, 159
Bruderer, S. 2013, A&A, 559, A46
Cutri, R. M., et al. 2012, yCat, 2311, 0
Fedele, D., Bruderer, S., van Dishoeck, E. F., et al. 2013, ApJL, 776, L3
Fedele, D., Pascucci, I., Brittain, S., et al. 2011, ApJ, 732, 106
Goto, M., van der Plas, G., van den Ancker, M., et al. 2012, A&A, 539, A81
Grady, C. A., Polomski, E. F., Henning, Th., et al. 2001, AJ, 122, 3396
Grady, C. A., Woodgate, B., Heap, S. R., et al. 2005, ApJ, 620, 470
Hein Bertelsen, R. P., Kamp, I., Goto, M., et al. 2014, A&A, 561, A102
Kley, W., & Dirksen, G. 2006, A&A, 447, 369
Le Bertre, T., & Winters, J. M. 1998, A&A, 334, 173
Liskowsky, J. P., Brittain, S. D., Najita, J. R., et al. 2012, ApJ, 760, 153
Liu, W. M., Hinz, P. M., Meyer, M. R., et al. 2003, ApJL, 598, L111
Lubow, S. H. 1991, ApJ, 381, 259
Malfait, K., Bogaert, E., & Waelkens, C. 1998a, A&A, 331, 211
Malfait, K., Waelkens, C., Waters, L. B. F. M., et al. 1998b, A&A, 332, L25
Mandell, A. M., Mumma, M. J., Blake, G. A., et al. 2008, ApJL, 681, L25
Mulders, G. D., Paardekooper, S.-J., Panić, O., et al. 2013, A&A, 557, A68
Panić, O., Ratzka, T., Mulders, G. D., et al. 2014, A&A, 562, A101
Pantin, E., Waelkens, C., & Lagage, P. O. 2000, A&A, 361, L9
Pontoppidan, K. M., Salyk, C., Blake, G. A., et al. 2010, ApJ, 720, 887
Quanz, S. P., Schmid, H. M., Geissler, K., et al. 2011, ApJ, 738, 23
Regály, Z., Sándor, Z., Dullemond, C. P., & van Boekel, R. 2010, A&A, 523, A69
Tatulli, E., Benisty, M., Ménard, F., et al. 2011, A&A, 531, A1
van der Plas, G., van den Ancker, M. E., Acke, B., et al. 2009, A&A, 500, 1137
van Leeuwen, F. 2007, A&A, 474, 653
Wright, E. L., Eisenhardt, P. R. M., Mainzer, A. K., et al. 2010, AJ, 140, 1868